Journal of Materials Chemistry C

PAPER

View Article Online
View Journal | View Issue

Cite this: J. Mater. Chem. C, 2018, 6, 3004

Significantly enhanced and precisely modeled thermal conductivity in polyimide nanocomposites with chemically modified graphene *via in situ* polymerization and electrospinning-hot press technology

Yongqiang Guo,†[a] Genjiu Xu,†[a] Xutong Yang,[a] Kunpeng Ruan,[a] Tengbo Ma,[a] Qiuyu Zhang,[a] Junwei Gu,*[ab] Yalan Wu,*[c] Hu Liu[de] and Zhanhu Guo*[e]

Received 28th January 2018,
Accepted 15th February 2018

DOI: 10.1039/c8tc00452h

rsc.li/materials-c

Both aminopropylisobutyl polyhedral oligomeric silsesquioxane (NH_2-POSS) and hydrazine monohydrate were utilized to functionalize graphene oxide (GO), and to obtain chemically modified graphene (CMG), which was then used for preparing thermally conductive CMG/polyimide (CMG/PI) nanocomposites *via* a sequential *in situ* polymerization and electrospinning-hot press technology. NH_2-POSS molecules were grafted on the GO surface, and CMG was obtained by the reaction between NH_2-POSS and GO. The thermal conductivity coefficient (λ), glass transition temperature (T_g) and heat resistance index (T_{HRI}) of the prepared CMG/PI nanocomposites were all increased with increasing the CMG loading. The λ value of the CMG/PI nanocomposites with 5 wt% CMG was significantly improved to 1.05 W m^{-1} K^{-1}, about 4 times higher than that of the pristine PI matrix (0.28 W m^{-1} K^{-1}). The corresponding T_g and T_{HRI} values were also increased to 213.0 and 282.3 °C, respectively. Moreover, an improved thermal conductivity model was proposed and predicted the λ values of the nanocomposites more precisely than those obtained from the typical Maxwell, Russell and Bruggemen classical models.

1. Introduction

With the rapid advances of light-emitting diodes (LEDs) towards higher integration and miniaturization, heat dissipation is a key factor in restraining their broader application.[1–5] However, the common cooling substrate of the LED lamp is basically aluminum or copper,[6,7] which usually possesses an inevitably high density, poor chemical resistance, *etc.* Under these circumstances, polymeric composites with a high thermal conductivity coefficient (λ) have been investigated actively to solve these problems.[8–13] Incorporating highly thermally conductive fillers into the polymeric matrix is regarded as one of the most economical and effective strategies to improve the λ of the polymers.[14–19] However, the improved λ value is still well below expectations. Moreover, the required high loading of thermally conductive fillers will deteriorate the mechanical properties, challenge the subsequent processing, and burden the weight of the polymeric composite finishings.[20–24] Therefore, it becomes a requirement to develop novel technologies for fabricating highly thermally conductive polymeric composites with reduced thermally conductive filler loadings.[25,26]

Compared with traditional fabrication methods (such as powder blending,[27] melt blending[28] and solvent blending,[29] *etc.*), *in situ* polymerization can be beneficial in improving the uniform dispersion of fillers in the polymeric matrix.[30–32] The electrospinning technique is another effective method to improve the uniform dispersion of fillers, and can also realize the effective alignment of fillers along with the oriented polymeric fibers,[33–35] in favor of shortening the contact distance between thermally conductive fillers, and finally to further increase the λ value at the same loading of fillers. In addition, the obtained electrospun fibers can be arranged in a specific orientation and followed by hot pressing to obtain the corresponding composites. Therefore,

[a] MOE Key Laboratory of Material Physics and Chemistry under Extraordinary Conditions, School of Science, Northwestern Polytechnical University, Xi' an, Shaanxi, 710072, P. R. China. E-mail: gjw@nwpu.edu.cn
[b] State Key Laboratory of Solid Lubrication, Lanzhou Institute of Chemical Physics, Chinese Academy of Sciences, Lanzhou, 730000, P. R. China
[c] PLA 323 Hospital, Xi'an, Shaanxi, 710054, P. R. China. E-mail: wuyalan@aliyun.com
[d] National Engineering Research Center for Advanced Polymer Processing Technology, Zhengzhou University, Zhengzhou 450002, P. R. China
[e] Integrated Composites Laboratory (ICL), Department of Chemical & Biomolecular Engineering, University of Tennessee, Knoxville, TN 37996, USA. E-mail: nanomaterials2000@gmail.com, zguo10@utk.edu
† The authors Yongqiang Guo and Genjiu Xu contributed equally to this work and should be considered co-first authors.

the combined method of *in situ* polymerization and electrospinning followed by hot-press technology becomes a promising method to effectively enhance the λ values of the polymeric composites with relatively lower thermally conductive filler loading.[36]

Polyimide (PI) possesses excellent heat resistance, good dimensional stability, outstanding chemical & temperature resistance, good mechanical properties, *etc.*[37–39] and thus has been widely applied in aerospace technology, electronics and other key fields.[40] However, the intrinsic low λ value of pristine PI matrix has limited its broader application.[41] Graphene presents an ultrahigh λ value (theoretical value, $\sim$5000 W m^{-1} K^{-1}),[42,43] which enables the potential to achieve high λ polymeric composites with a relatively lower graphene loading. However, the near-perfect graphene is usually hard to disperse uniformly in a polymeric matrix.[44] The poor processability of graphene has precluded its large-scale practical applications. Owing to the presence of lots of oxygen-containing groups (–COOH, –OH, –O–) on the surface and edges of graphene oxide (GO),[45] chemically modified graphene (CMG) with different chemical compositions can be engineered and obtained by means of covalent bonds formed between GO and the modifier. Examples include the incorporation of (3-aminopropyl)trimethoxysilane (APTS),[46] 1-(3-aminopropyl)-3-methylimidazolium bromide,[47] octa(aminophenyl)-silsesquioxane (OAPS),[48] and methyl methacrylate (MMA)[49] on GO to increase its solubility in organic solvents. Nevertheless, only a rather limited thermal stability and solubility has been realized by modifying GO with organic groups. On the other hand, polyhedral oligomeric silsesquioxane (POSS) contains eight organic groups surrounding a cage-like inorganic core that consists of Si–O–Si bonds. Therefore, POSS combines the advantages of both the organic merits like high reactivity and high solubility in many solvents, and inorganic merits such as high thermal stability and strength. Despite studies reported utilizing POSS to modify graphene to improve graphene's solubility in organic solvents,[50,51] using POSS modified graphene as thermally conductive fillers to improve the thermal conductivity has seldom been investigated in polymeric composites. In addition, although graphene or CMG has been added to the PI matrix, the corresponding thermal conductivity enhancement is still low. For example, Yang *et al.*[52] fabricated a graphene/polyimide hybrid film with a 21.9% enhancement in the in-plane thermal conductivity. Feng *et al.*[53] prepared a KH-550 modified graphene/polyimide composite with about 3 times higher thermal conductivity than that of the PI matrix. Therefore, to improve the thermal conductivity is still a challenge.

In the present work, we designed and fabricated highly thermally conductive CMG/PI nanocomposites using *in situ* polymerization followed by electrospinning-hot press technology. CMG was obtained by functionalizing the GO surface *via* combining the modification and reduction of aminopropylisobutyl polyhedral oligomeric silsesquioxane (NH_2-POSS) and hydrazine monohydrate. Static precipitation, X-ray photoelectron spectroscopy (XPS), Fourier transform infrared (FTIR), thermogravimetry (TG), Raman and transmission electron microscopy (TEM) methods were performed to characterize the surface components and properties of GO and CMG. The mass fraction of CMG fillers affecting the thermal conductivities and thermal properties of the CMG/PI composites was also investigated. Furthermore, based on heat energy conservation and modified effective medium theory, an improved thermal conductivity model was also proposed and employed to calculate the obtained experimental λ values of the anisotropic CMG/PI composites.

2. Materials and methods

2.1. Materials

Bis-(3-phthalyl anhydride) ether (ODPA) and *N*,*N*-diisopropylcarbodiimide (DIC) were received from Sun Chemical Technology (Shanghai) Co., Ltd, China; 1,3-bis(4-aminophenyloxy)benzene (APB) was purchased from Changzhou Sunlight Medicine Raw Material Co., Ltd, China. ODPA and APB were sublimed at sub-atmospheric pressure and then dried at 100 °C for 2 h in a vacuum oven under −0.1 MPa. Natural graphite flake, 325 mesh, was supplied from Alfa Aesar (China) Co., Ltd, China. Aminopropylisobutyl polyhedral oligomeric silsesquioxane (NH_2-POSS) was received from Hybrid Plastics Co. (Hattiesburg, USA). Hydrazinium hydrate solution (80%) was received from Tianjin Chemical Reagent Co., Ltd China; absolute ethanol, tetrahydrofuran (THF) and dimethylacetamide (DMAc) were all supplied from Tianjin Tianli Chemical Co., Ltd, China. THF and DMAc were distilled to remove water and followed by adding molecular sieves type 4A.

2.2. Fabrication of thermally conductive CMG/PI nanocomposites

GO Preparation. GO was prepared by acid oxidation of graphite powder according to the modified Hummers method.[54] Briefly, one gram graphite and 30 mL sulfuric acid (98%) were added into an anhydrous three-necked flask. 3 g $KMnO_4$ was then slowly added into the above flask at 0 °C and kept stirring for 2 h at 35 °C. After adding a small quantity of water, the mixture was stirred at 85 °C for 15 min and then 15 mL H_2O_2 was added. The mixture was centrifuged, washed consecutively with HCl and distilled water, and then dried by vacuum freeze drying.

CMG preparation. Briefly, 0.5 g GO and 1.5 g DIC were added into 500 mL THF in a beaker, followed by ultrasonic treatment for 2 h. The obtained mixture was poured into an anhydrous three-necked flask followed by adding 1 g NH_2-POSS, and then kept stirring for 48 h at 65 °C. After that, 0.5 g hydrazinium hydrate solution was added into the above flask and then kept stirring for another 8 h. The mixture was centrifuged and washed by distilled water and underwent further drying.

Fabrication of CMG/PI Nanocomposites. Thermally conductive CMG/PI nanocomposites were fabricated by the method of *in situ* polymerization followed by electrospinning-hot press technology. Fig. 1 presents the corresponding schematic diagram of the fabrication for the CMG/PI nanocomposites. Briefly, a certain amount of CMG was poured into the mixed solvent (DMAc/THF = 2/3, wt/wt) with ultrasonic treatment for 1 h and then 0.5 mmol APB was added. The mixture was added into a three-necked flask with an inlet for nitrogen purging and a mechanical stirrer. 0.5 mmol ODPA was then added into the

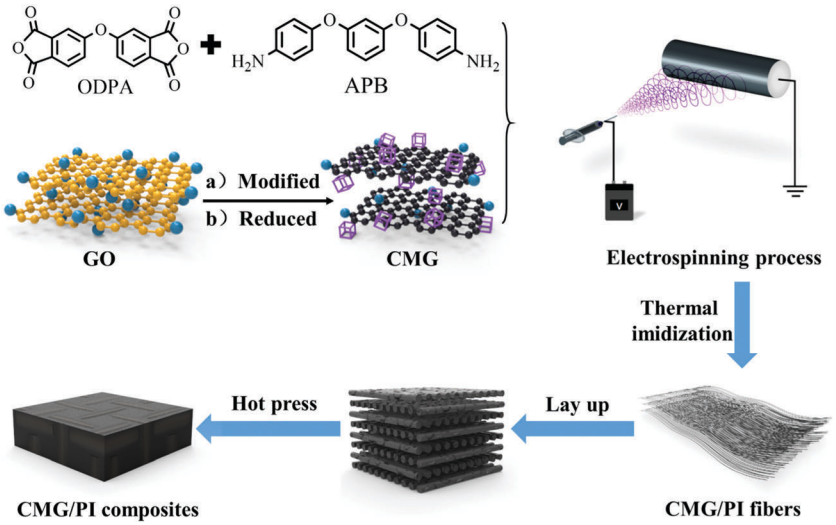

Fig. 1 Schematic diagram of the fabrication of the CMG/PI nanocomposites.

above flask in several batches and then kept stirring for another 3 h at 0 °C to obtain CMG/PAA. The homogenous mixture of CMG/PAA was then enclosed in a 10 mL syringe with a stainless steel needle. The optimized parameters of the electrospinning process were obtained as follows. The loaded voltage and distance between the needle and rolling collector were set as 20 kV and 30 cm, respectively. The obtained CMG/PAA fibers were firstly put into a vacuum oven at 80 °C for 4 h, then treated *via* thermal-imidization according to the following procedures: 120 °C/1 h + 200 °C/1 h + 250 °C/1 h, to obtain the CMG/PI fibers. The CMG/PI fibers were laminated and then hot pressed at 320 °C under 10 MPa for 40 min. Finally the thermally conductive CMG/PI nanocomposites were fabricated.

2.3. Characterization

Scanning electron microscope (SEM) morphologies of the samples were analyzed by VEGA3-LMH (TESCAN Corp., Czech Republic). Fourier transform infrared (FTIR) spectra were obtained on a Bruker Tensor 27 equipment (Bruker Corp., Germany). The thermal conductivity coefficient (λ) and thermal diffusivity (α) values of the samples (20 mm × 20 mm × 2 mm) were measured using a TPS2200 Hot Disk instrument (AB Corp., Sweden) by the transient plane source method according to standard ISO 22007-2: 2008. During the testing process, a probe with bifilar spiral as a heating/sensing element was sandwiched between two specimens with flat surfaces, and the probe was oriented in the fiber direction. A heat pulse and a dynamic temperature fields in the specimens were formed by an electrical current pulse through the probe, the heat flux was transferred by radiation inside the specimens. In addition, the isotropic mode was also chosen in our actual testing process. The thermal images of the samples were taken immediately by a Fluke infrared thermal imager (Ti 27), by placing the samples on a hot plate (Linkam GS315) at a constant temperature 90 °C. Differential scanning calorimetry (DSC) analyses of the samples were carried out at 10 °C min^{-1} (nitrogen atmosphere), over the whole temperature range of 40–300 °C by DSC1 (Mettler-Toledo Corp., Switzerland). Thermal gravimetric (TG) analyses of the samples were carried out by using a STA 449F3 (NETZSCH C Corp., Germany) at 10 °C min^{-1} (argon atmosphere), over the whole temperature range of 40–1000 °C. The contact angles between CMG and PI fibers were measured by using a CA100B (Shanghai Innuo Precision Instruments Co., Ltd) at room temperature. X-ray photoelectron spectroscopy (XPS) analyses of the samples were carried out by using a K-Alpha equipment (Thermo Electron Corp., USA) to measure the elemental components on the surface of GO and CMG. Transmission electron microscopy (TEM) was performed on a Tecnai F30G (FEI Corp., USA). Raman spectra were collected by a using a Reflex Raman Microscope and Spectrometer (Renishaw, UK) with a 514 nm laser, GO and CMG powders were placed on a clean glass slide and pressed slightly.

3. Results and discussion

3.1. Characterization of GO and CMG

Fig. 2 shows the dispersion states of GO and CMG in different solvents. GO presents a strong hydrophilicity due to the presence of lots of hydrophilic groups on its surface and edge (Fig. 2a). After surface functionalization, CMG enters the oil phase from the aqueous phase (Fig. 2b). The reason is that the organic groups in the NH_2-POSS molecules can react with the oxygen-containing groups (epoxy and carboxyl groups) on the GO surface,[55] and thus CMG becomes more soluble in organic solvents. In addition, the introduction of NH_2-POSS can also provide a better compatibility between CMG and THF, in favor of preventing the CMG from precipitating due to van der Waals' force, finally good stability is maintained for more than 24 h (Fig. 2b′ and b″).

Fig. 3 shows the FTIR (a), TGA (b) and XPS (c) curves of GO and CMG. In Fig. 3a, GO presents the corresponding characteristic absorption peaks of the hydroxyl (3430 cm^{-1}), carboxyl (1620 cm^{-1}), and epoxy (1230 cm^{-1}) groups.[45] After surface functionalization,

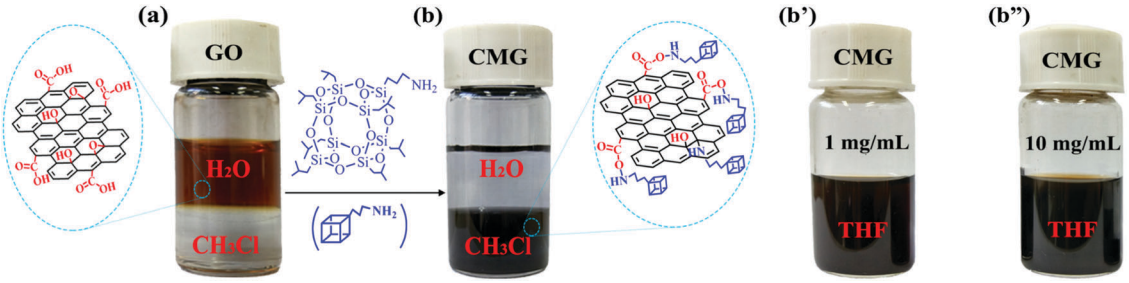

Fig. 2 The dispersion states of GO and CMG in different solvents.

the above three peaks of CMG in the corresponding position are all weakened. In addition, a new characteristic absorption peak (Si–O–Si) at 1100 cm^{-1} appears, and another two characteristic absorption peaks from 2800 to 2900 cm^{-1} also appear, mainly ascribed to the isobutyl groups in NH_2-POSS. CMG presents a much higher thermal stability than that of GO (Fig. 3b). The main reason is that the cage structure of NH_2-POSS with the alternate Si–O skeleton possesses a relatively higher bond energy. From Fig. 3c, compared to that of GO, there are new peaks of N 1s, Si 2s, and Si 2p (399 eV, 150 eV, 99 eV, respectively) in the XPS spectra of CMG.[55] Moreover, the COOH peak at 289 eV of GO disappears and the intensity of C–O (286 eV) and C═O (288 eV) peaks is also decreased (Fig. 3c′ and c″).

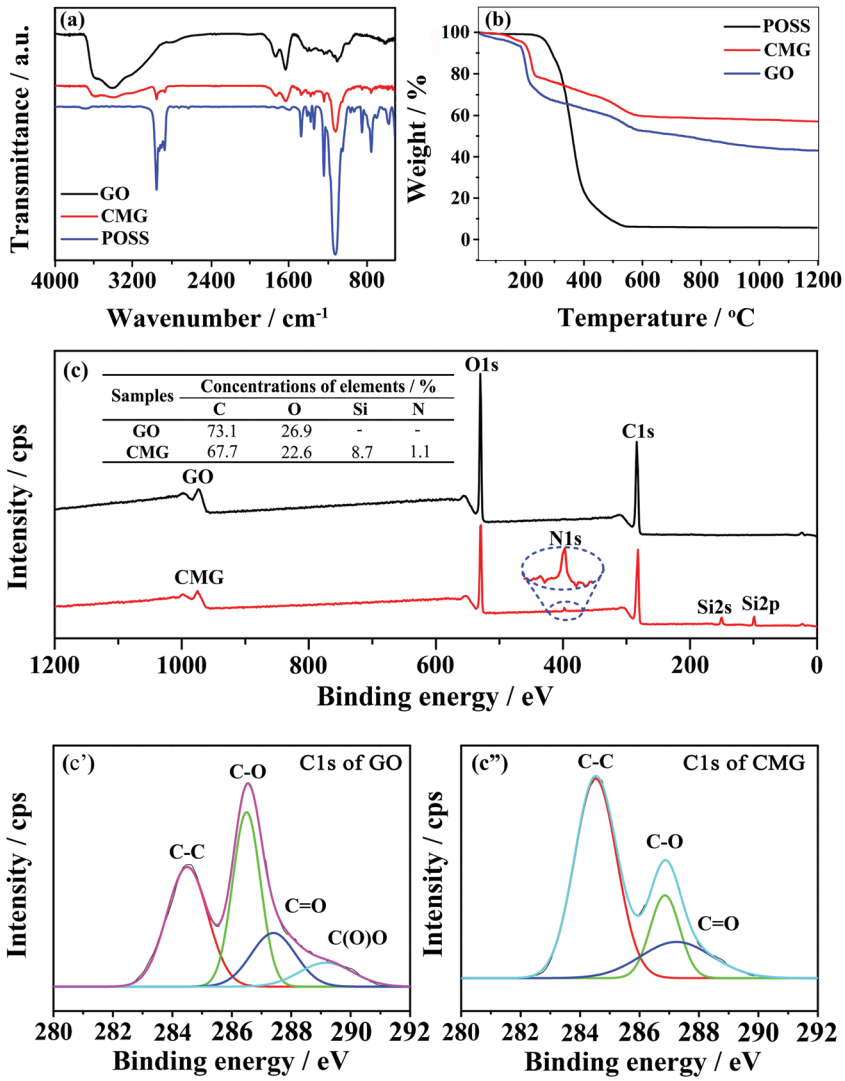

Fig. 3 FTIR, TGA and XPS curves of GO and CMG. (a) FTIR spectra of GO, CMG, POSS (b) TGA curves for GO, CMG, POSS (c) XPS spectra of GO and CMG and high-resolution XPS spectra of C 1s for (c′) GO and (c″) CMG.

This is attributed to the amino groups on the NH_2-POSS being able to react with the epoxy and carboxyl groups on the surface of GO.[55] Meanwhile, the weakening intensity of the C–O and C═O peaks is also partly attributed to the hydrazine hydrate being able to further reduce the oxygen-containing groups.[56] FTIR, TGA and XPS analyses indicate that NH_2-POSS has been successfully grafted onto the surface of GO.

Fig. 4 shows the Raman spectra and TEM images of GO and CMG. GO and CMG present an obvious D peak at 1350 cm^{-1} (Fig. 4a), ascribed to the intrinsic defects. Herein, the intensity of the D peak in CMG is stronger than that of GO. It is mainly attributed to the introduced NH_2-POSS molecules being able to induce the structural distortion and lattice expansion of GO. As for the sp^2 carbons in graphene, the feature of the G' peak in Raman spectrum is ascribed to the double resonance Raman process, and is also related to the electron and phonon dispersion conditions. The line shape of the G' peak depends on the stack feature and numbers of graphene layers. Moreover, the increase of the graphene layers can cause a blue shift and full width at half maximum (FWHM) widening of the G' peak.[57] As shown in Fig. 4a′, the G' peak presents an obvious blue shift and widened FWHM (compared with the monolayer graphene[57]), and it can be fitted into three Lorentzian peaks due to the divided electron band structure. These multiple Lorentzian peaks indicate that CMG contains at least four layers. As shown in Fig. 4b, the GO sheets exhibit a cicada's wings structure and appear wrinkled. Compared with GO, CMG exhibits a rougher structure (Fig. 4c), there are lots of black particulates on the surface of CMG. And the particulate size is consistent with that of NH_2-POSS. This further demonstrates that NH_2-POSS has been successfully grafted onto the GO surface.

3.2. SEM images of pristine PI fibers and CMG/PI fibers

Fig. 5 shows the SEM images of the pristine PI fibers and CMG/PI fibers. The diameters of the pristine PI fibers and CMG/PI fibers are uniform. Moreover, the surface of the pristine PI fibers is smooth, while the surface of CMG/PI fibers becomes rougher due to the increasing addition of CMG. In addition, CMG is coated on the CMG/PI fiber surface. There is no adhesion between CMG/PI fibers. CMG is also evenly distributed on the surface of the CMG/PI fibers. The contact angles of the pristine PI fibers and CMG/PI fibers are also shown in Fig. 6. The hydrophobicity of the CMG/PI fibers is increased with increasing the CMG loading, mainly attributed to the hydrophobic performance of the NH_2-POSS molecules.

3.3. Properties of the CMG/PI nanocomposites

Fig. 7 shows the influence of CMG mass fraction on the λ and α value of the CMG/PI nanocomposites. A nonlinear increase in the λ and α value of the CMG/PI nanocomposites is observed with increasing the CMG loading. And the λ and α values of the CMG/PI nanocomposite with 5 wt% CMG are significantly improved to 1.05 W m^{-1} K^{-1} and 0.98 mm^2 s^{-1}, about 4 times higher than that of the pristine PI matrix (λ of 0.28 W m^{-1} K^{-1} and α of 0.24 mm^2 s^{-1}), respectively. The main reason is that a small amount of CMG is dispersed randomly and there is seldom interaction between CMG particles, resulting in a slight improvement in the λ and α values. With increasing the mass

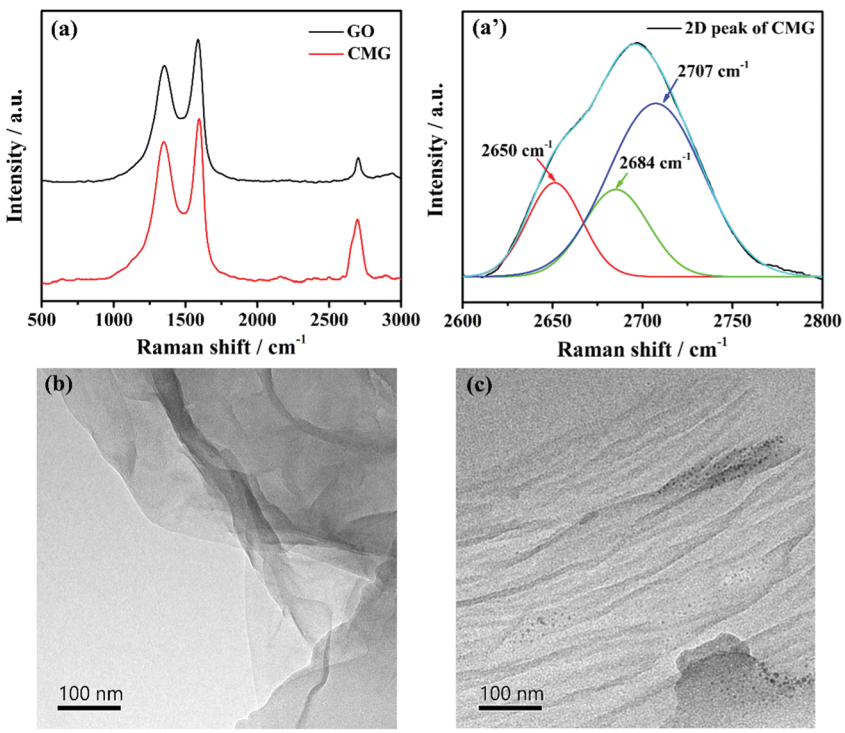

Fig. 4 Raman spectra and TEM images of GO and CMG. (a) Raman spectra of GO and CMG and 2D peak for (a′) CMG (b) TEM image of GO (c) TEM image of CMG.

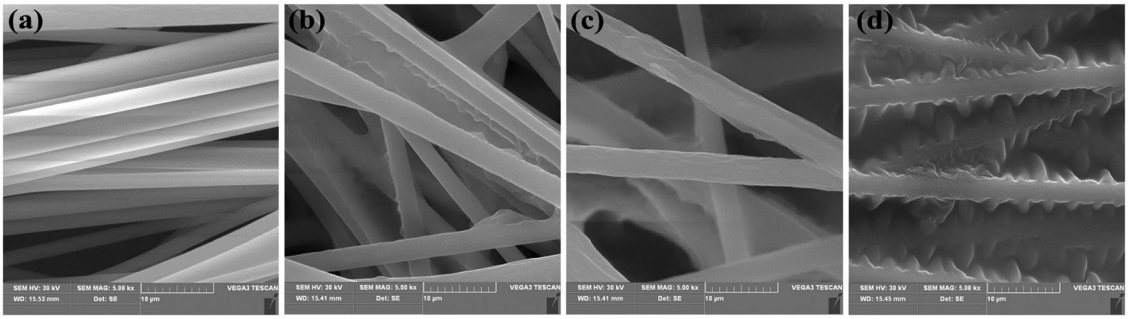

Fig. 5 SEM images of pristine PI fibers and CMG/PI fiber (a) pristine PI fibers (b) 1 wt% CMG/PI fibers (c) 3 wt% CMG/PI fibers (d) 5 wt% CMG/PI fibers.

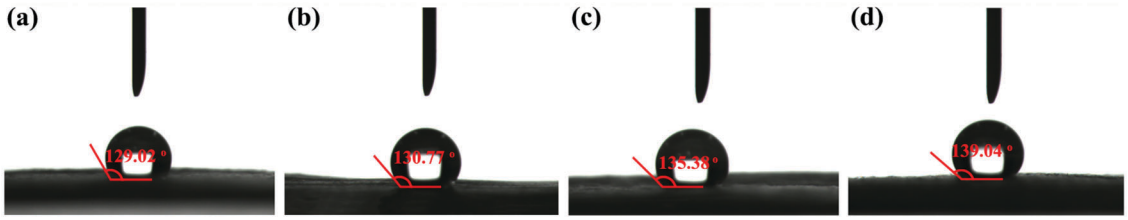

Fig. 6 Contact angles of pristine PI fibers and CMG/PI fibers. (a) pristine PI fibers (b) 1 wt% CMG/PI fibers (c) 3 wt% CMG/PI fibers (d) 5 wt% CMG/PI fibers.

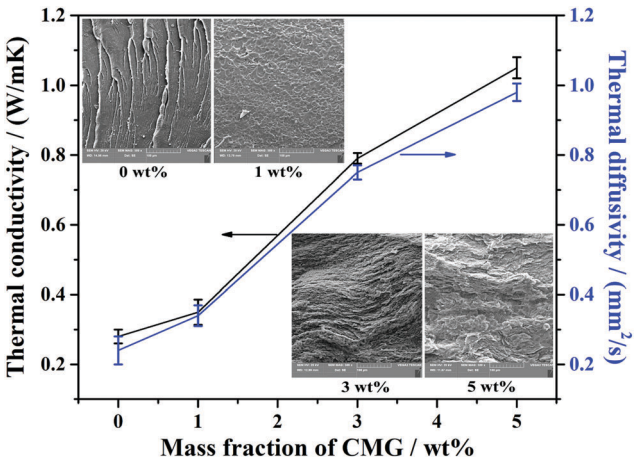

Fig. 7 Mass fraction of CMG influence on the λ value of the CMG/PI nanocomposites. The inset SEM images was the fracture surfaces of PI and CMG/PI nanocomposites.

fraction of CMG, some CMG–CMG contacts in certain regions appear. And the effective thermally conductive channels & networks of CMG–CMG can be formed with further increasing CMG loading, resulting in an obvious improvement of λ and α values.

Fig. 8 shows the corresponding infrared thermal images of the CMG/PI nanocomposites. The surface temperature of the CMG/PI nanocomposites is increased faster with a relatively higher CMG loading, indicating a higher λ value and a better thermal diffusion, which is also well consistent with the experimental results from Fig. 7. Moreover, the temperature distribution on the surface of each sample is uniform, revealing that the CMG maintains a macroscopic uniform dispersibility. Table 1 presents the obtained λ value of the polymeric composites filled with various thermally conductive fillers obtained from other literature.[15,58–62] Compared to other studies, the fabricated nanocomposites in our work display a relatively higher λ value at the same thermally conductive filler loading. The main reasons are listed as follows. (1) CMG itself has an ultrahigh λ value, and can transfer heat much easier; (2) CMG particles more easily overlap with each other in the polymeric matrix and significantly reduces the thermally conductive threshold for a given filler loading; (3) improved dispersion of CMG and interfacial compatibility of CMG/PI are more beneficial for forming effective thermally conductive networks and decreasing the interfacial thermal barrier; (4) our proposed fabrication method of *in situ* polymerization followed by the electrospinning process can further improve the uniform dispersion of CMG in the PI matrix,[30–32] also effectively reducing the thermally conductive threshold.

However, there is still no definite model or equation for comparing the λ values of the isotropic and anisotropic polymeric nanocomposites.[63,64] Modified effective medium theory has been widely used to model the thermal conductivity of polymeric nanocomposites in the parallel and perpendicular directions.[65–67] Based on the modified effective medium theory and heat energy conservation, considering the following comprehensive factors, such as thickness, geometrical factor, orientation distribution & volume fraction of CMG, the thermal resistance & thickness of the CMG/PI interface layer, and the intrinsic λ value of the CMG and PI matrix, the correlative model for the CMG/PI nanocomposites is deduced and built in our work.

For laminate nanocomposites, the matrix containing parallel fillers is assumed to be oriented perpendicular to the X_{33} axis (Fig. 9a). The corresponding thermal conductivity equation of anisotropic polymeric nanocomposites can be expressed as an ellipsoid equation by mathematical treatment. The geometrical

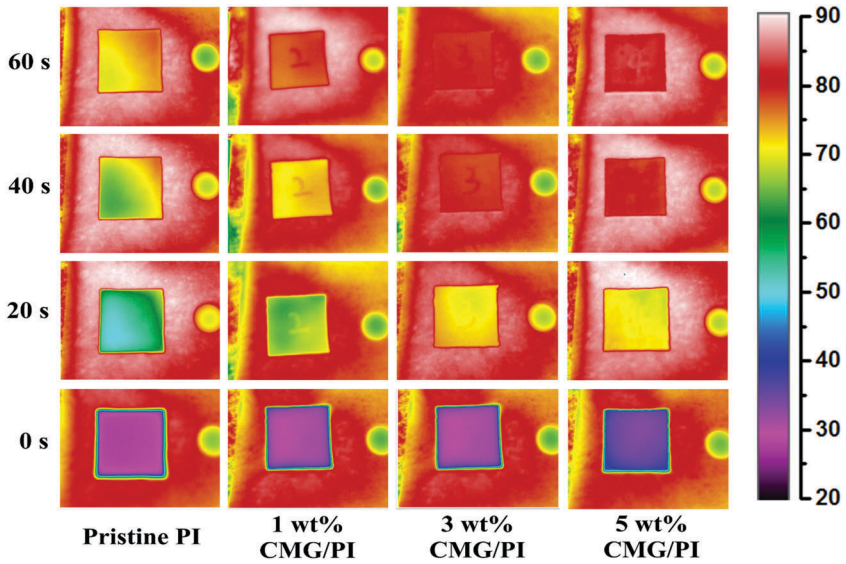

Fig. 8 Infrared thermal images of the CMG/PI nanocomposites.

Table 1 A comparison of the enhanced λ value for different polymeric composites

Filler composition & loading	Polymeric matrix	λ (W m^{-1} K^{-1})	Enhancement (%)	Ref.
5 wt% CMG	Polyimide	1.05	275	Our work
5 wt% GNPs	Epoxy	0.68	162	58
6 wt% GNPs	Polypropylene	0.83	84	59
7 wt% GNPs	Polyethylene	1.08	116	60
3 wt% RGO	Styrene-butadiene rubber	0.27	17	61
3 phr mSiO$_2$@rGO	Styrene-butadiene rubber	0.42	83	62
5 wt% BN	Polyphenylene sulfide	0.4	74	15

significance of thermal conductivity for anisotropic polymeric nanocomposites is shown in Fig. 9b, meaning the presence of different heat fluxes along different directions.

The modified effective medium theory is adopted to model the thermal conductivity of CMG/PI nanocomposites.[68]

$$\lambda_{11}^{*} = \lambda_{22}^{*} = \lambda_{\mathrm{m}}\frac{2+V_{\mathrm{f}}\left[\beta_{11}(1-L_{11})\left(1+\left\langle\cos^2\theta\right\rangle\right)+\beta_{33}(1-L_{33})\left(1-\left\langle\cos^2\theta\right\rangle\right)\right]}{2-V_{\mathrm{f}}\left[\beta_{11}L_{11}\left(1+\left\langle\cos^2\theta\right\rangle\right)+\beta_{33}L_{33}\left(1-\left\langle\cos^2\theta\right\rangle\right)\right]} \quad (1a)$$

$$\lambda_{33}^{*} = \lambda_{\mathrm{m}}\frac{1+V_{\mathrm{f}}\left[\beta_{11}(1-L_{11})\left(1-\left\langle\cos^2\theta\right\rangle\right)+\beta_{33}(1-L_{33})\left\langle\cos^2\theta\right\rangle\right]}{1-V_{\mathrm{f}}\left[\beta_{11}L_{11}\left(1-\left\langle\cos^2\theta\right\rangle\right)+\beta_{33}L_{33}\left\langle\cos^2\theta\right\rangle\right]} \quad (1b)$$

with

$$\beta_{ii} = \frac{\lambda_{ii}^{\mathrm{c}}-\lambda_{\mathrm{m}}}{\lambda_{\mathrm{m}}+L_{ii}\left(\lambda_{ii}^{\mathrm{c}}-\lambda_{\mathrm{m}}\right)} \quad (2)$$

$$\left\langle\cos^2\theta\right\rangle = \frac{\int\rho(\theta)\cos^2\theta\sin\theta\mathrm{d}\theta}{\int\rho(\theta)\sin\theta\mathrm{d}\theta} \quad (3)$$

where λ_{11}* and λ_{22}* represent the in-plane thermal conductivities of the nanocomposites, λ_{33}* represents the through-plane thermal conductivity of the nanocomposites, λ_{m} denotes the thermal conductivity of the polymeric matrix. θ is the angle between the CMG symmetric axis and the perpendicular direction of the nanocomposites. $\rho(\theta)$ is a distribution function describing the CMG orientation. $\langle\rangle$ represents spatial averaging. V_{f} is the volume fraction of CMG. $\lambda_{ii}^{\mathrm{c}}(i = 1, 2, 3)$ is the equivalent thermal conductivity along the X_{ii}' symmetric axis of the composite unit cell. L_{ii} $(i = 1, 2, 3)$ is a well-known geometrical factor dependent on the CMG shape. $\lambda_{ii}^{\mathrm{c}}$ and L_{ii} are shown by the following equations:

$$L_{11} = L_{22} = \begin{cases} \dfrac{P^2}{2(P^2-1)} - \dfrac{P}{2(P^2-1)^{\frac{3}{2}}}\cosh^{-1}P, & P > 1 \\ \dfrac{P^2}{2(P^2-1)} + \dfrac{P}{2(P^2-1)^{\frac{3}{2}}}\cos^{-1}P, & P < 1 \end{cases} \quad (4)$$

$$L_{33} = 1 - 2L_{11} \quad (5)$$

$$\lambda_{ii}^{\mathrm{c}} = \frac{\lambda_{\mathrm{f}}}{1+\gamma L_{ii}\frac{\lambda_{\mathrm{f}}}{\lambda_{\mathrm{m}}}} \quad (6)$$

with

$$\gamma = \begin{cases} \left(2+\dfrac{1}{P}\right)\dfrac{R_{\mathrm{Bd}}\lambda_{\mathrm{m}}}{l}, & P > 1 \\ (1+2P)\dfrac{R_{\mathrm{Bd}}\lambda_{\mathrm{m}}}{h}, & P < 1 \end{cases} \quad (7)$$

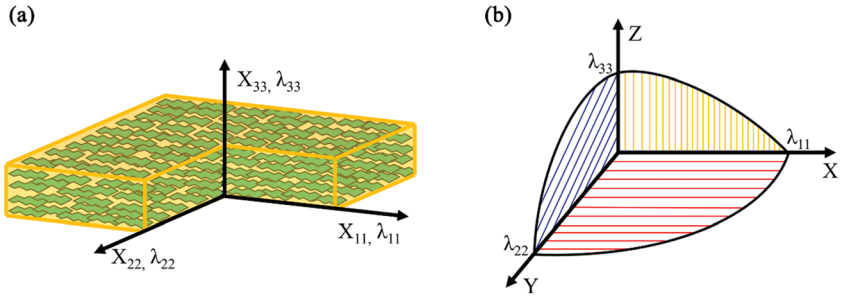

Fig. 9 (a) Schematic of the laminate structure of the CMG/PI nanocomposites and (b) heat flux in the anisotropic polymeric nanocomposites.

where R_{Bd} represents the interfacial resistance (known as the Kapitza resistance[69]) between CMG and the PI matrix, and h is the thickness of CMG.

For CMG, $P \to 0$, then $L_{11} = L_{22} = 0$, $L_{33} = 1$. And the following equations can be obtained:

$$\lambda_{11}^{c} = \lambda_{22}^{c} = \lambda_f \tag{8}$$

$$\lambda_{33}^{c} = \frac{\lambda_f}{1 + \frac{R_{Bd}\lambda_f}{h}} \tag{9}$$

$$\beta_{11} = \beta_{22} = \frac{\lambda_f}{\lambda_m} - 1 \tag{10}$$

$$\beta_{33} = 1 - \frac{R_{Bd}\lambda_m}{h} - \frac{\lambda_m}{\lambda_f} \tag{11}$$

The eqn (1a) and (1b) can be reduced as follows:

$$\lambda_{11}^{*} = \lambda_{22}^{*} = \lambda_m \frac{2 + V_f\left[\left(\frac{\lambda_f}{\lambda_m} - 1\right)\left(1 + \langle\cos^2\theta\rangle\right)\right]}{2 - V_f\left[\left(1 - \frac{R_{Bd}\lambda_m}{h} - \frac{\lambda_m}{\lambda_f}\right)\left(1 - \langle\cos^2\theta\rangle\right)\right]} \tag{12a}$$

$$\lambda_{33}^{*} = \lambda_m \frac{1 + V_f\left[\left(\frac{\lambda_f}{\lambda_m} - 1\right)\left(1 - \langle\cos^2\theta\rangle\right)\right]}{1 - V_f\left[\left(1 - \frac{R_{Bd}\lambda_m}{h} - \frac{\lambda_m}{\lambda_f}\right)\langle\cos^2\theta\rangle\right]} \tag{12b}$$

In this work, a more accurate model has been developed to model the thermal conductivity of the CMG/PI nanocomposites. To our knowledge, the thermal conductivity of graphene is far higher than that of the PI matrix. Thus, the $\frac{\lambda_f}{\lambda_m}$ value is considerably larger than 1, and the $\frac{\lambda_m}{\lambda_f}$ value is close to 0. On the other hand, the thermal conductivity of graphene varies with the changing graphene layer. We replace h with an average thickness ($\bar{h}$) and use the average graphene thermal conductivity ($\bar{\lambda}_f$) to substitute the λ_f. Thus eqn (12a) and (12b) are reduced to:

$$\lambda_{11}^{*} = \lambda_{22}^{*} = \lambda_m \frac{2 + V_f\left[\frac{\bar{\lambda}_f}{\lambda_m}\left(1 + \langle\cos^2\theta\rangle\right)\right]}{2 - V_f\left[\left(1 - \frac{R_{Bd}\lambda_m}{\bar{h}}\right)\left(1 - \langle\cos^2\theta\rangle\right)\right]} \tag{13a}$$

$$\lambda_{33}^{*} = \lambda_m \frac{1 + V_f\left[\frac{\bar{\lambda}_f}{\lambda_m}\left(1 - \langle\cos^2\theta\rangle\right)\right]}{1 - V_f\left[\left(1 - \frac{R_{Bd}\lambda_m}{\bar{h}}\right)\langle\cos^2\theta\rangle\right]} \tag{13b}$$

In our work, ρ_f is widely accepted as 2.21 g cm^{-3}, $\bar{\lambda}_f$ is measured and is about 120 W m^{-1} K^{-1}, $\bar{h}$ is approximately 1.5 nm, ρ_m is about 1.36 g cm^{-3}, λ_m is 0.28 W m^{-1} K^{-1}, θ is about 5°, obtained from the SEM in Fig. 7, R_{Bd} is about 7.8 × 10^{-8} (m^2 K) W^{-1}, obtained from the reports about graphene.[68] As a result, the thermal conductivities of the CMG/PI nanocomposites in the parallel and perpendicular directions are obtained, respectively. Furthermore, the heat conduction is not limited in one direction, so that the thermal conductivity is a vector that varies with direction for any point in the anisotropic CMG/PI nanocomposites. However, it is impractical to calculate the thermal conductivity for any point in the anisotropic CMG/PI nanocomposites. Therefore, transferring the anisotropic thermal conductivity into isotropic thermal conductivity and calculating the effective thermally conductive coefficient are effective methods to model the thermal conductivities of the CMG/PI nanocomposites.

In the field of heat transfer, thermal energy is the heat transfer in a given area in a certain time, denoted as Q.

$$Q = \int q_n \tau \mathrm{d}A \tag{14}$$

where q_n is the heat flux in the normal direction of the given area A, and τ is a certain period time.

In our proposed thermal conductivity model, we assume that the thermally conductive geometry of the anisotropic CMG/PI nanocomposites is an ellipsoid, and the corresponding semi-major axes are λ_{11}, λ_{22}, λ_{33}. Meanwhile, we define the effective thermal conductivity coefficient of the isotropic polymeric nanocomposites as λ' and the thermally conductive geometry is a sphere, and the corresponding radius is λ'. In addition, we consider the corresponding thermally conductive geometry as one of the parts in a semi-infinite object. In mathematics, semi-infinite objects are infinite or unbounded in some but not all possible ways. In physics, if there is a zone where the initial temperature remains unchanged during time $\tau = 0$ to $\tau = \tau$ when the boundary temperature has a sudden change on an object, and the object can be considered as a semi-infinite object. The semi-infinite object to model the

thermal conductivity can satisfy our actual thermal test method (plane source method).

The heat flux is defined as follows:[70]

$$q_n = c\frac{\lambda\left[t_{(x,\tau)} - t_i\right]}{\sqrt{\alpha\tau}} \quad (15)$$

where c is a constant, $t_{(x,\tau)}$ is the temperature distribution in the semi-infinite object and is defined as follows:

$$t_{(x,\tau)} = (t_w - t_i)\left(1 - \frac{z}{\sqrt{12\alpha\tau}}\right)^2 \quad (16)$$

where t_w is the boundary temperature and t_i is the initial temperature, $t_w > t_i$. α is the thermal diffusivity value and is defined $\alpha = \frac{\lambda}{\rho_c c_c}$. ρ_c and c_c is the density and specific heat capacity of the CMG/PI nanocomposites, respectively.

Taking the vertex of the ellipsoidal pole radius as the origin of the coordinates, the corresponding function can be expressed as:

$$\frac{x^2}{{\lambda_{11}}^2} + \frac{y^2}{{\lambda_{22}}^2} + \frac{(z-\lambda_{33})^2}{{\lambda_{33}}^2} = 1 \quad (17)$$

The given area A in eqn (14) is the intersection of the plane perpendicular to the polar radius and the ellipsoid, and the area of the intersection is expressed as follows:

$$A = \pi\lambda_{11}\lambda_{22}\left[1 - \frac{(z-\lambda_{33})^2}{{\lambda_{33}}^2}\right] \quad (18)$$

As a result, the thermal energy in the ellipsoid can be expressed as follows, denoted as Q_1:

$$Q_1 = \int_0^{2\lambda_{33}} c\frac{\lambda_{33}\left[(t_w - t_i)\left(1 - \frac{z}{\sqrt{12\alpha\tau}}\right)^2 - t_i\right]}{\sqrt{\alpha\tau}}\pi\lambda_{11}\lambda_{22}\left[1 - \frac{(z-\lambda_{33})^2}{{\lambda_{33}}^2}\right]\tau dz \quad (19)$$

In the same way, the thermal energy in the sphere is denoted as Q_2, expressed as follows:

$$Q_2 = \int_0^{2\lambda'} c\frac{\lambda'\left[(t_w - t_i)\left(1 - \frac{z}{\sqrt{12\alpha\tau}}\right)^2 - t_i\right]}{\sqrt{\alpha\tau}}\pi{\lambda'}^2\left[1 - \frac{(z-\lambda')^2}{{\lambda'}^2}\right]\tau dz \quad (20)$$

The effective thermal conductivity coefficient λ' can be obtained letting $Q_1 = Q_2$.

$$\lambda' \approx \left\{\frac{3\lambda_{11}\lambda_{22}\int_0^{2\lambda_{33}}\sqrt{\lambda_{33}}\left[(t_w - t_i)\left(1 - \frac{z}{\sqrt{12\alpha\tau}}\right)^2 - t_i\right]\left[1 - \frac{(z-\lambda_{33})^2}{{\lambda_{33}}^2}\right]dz}{4(t_w - 2t_i)}\right\}^{\frac{2}{7}} \quad (21)$$

For CMG/PI nanocomposites, ρ_c is widely accepted as 1.37 g cm^{-3}, c_c is approximately 1.2 J (kg K)$^{-1}$. The others parameters such as τ, t_w and t_i can be obtained by the hot-disk.

The experimental λ values of the CMG/PI nanocomposites and the theoretical λ values obtained from our proposed thermal conductivity model, and the Maxwell, Russell and Bruggemen models are shown in Fig. 10. The obtained λ values from our proposed thermal conductivity model are more consistent with the experimental λ values than those of the other three classical theory models. This can confirm that our proposed thermal conductivity model can be promising to calculate the effective thermal conductivity coefficient (ETC) of the anisotropic polymeric nanocomposites.

DSC and TGA curves of the pristine PI matrix and CMG/PI nanocomposites are shown in Fig. 11, and the corresponding characteristic thermal data are presented in Table 2. The T_g value of the CMG/PI nanocomposites is increased with increasing the CMG loading, and the T_g value of the CMG/PI nanocomposite with 5 wt% CMG is enhanced from 205.9 °C for the pristine PI matrix to 213.0 °C. On one hand, the PI molecular chain can be oriented and aligned during the electrospinning process. On the other hand, the existence of CMG might increase the rigidity of the PI molecular chains, and thus restrict the thermal motion.[71,72] With increasing the CMG loading, the limitation of movement is also increased, and the glass transition zone also becomes more and more inconspicuous accordingly. As also seen from Fig. 10 and Table 2, compared to that of the pristine PI matrix, with the increasing CMG loading, the corresponding thermal decomposition temperature (T_5 and T_{30}) and the $T_{\text{Heat resistance index}}$ (T_{HRI})[73] values of the CMG/PI nanocomposites are all enhanced. And the $T_{\text{Heat resistance index}}$ (T_{HRI}) value of the CMG/PI nanocomposite with 5 wt% CMG is enhanced from 270.7 °C for the pristine PI matrix to 282.3 °C. In addition, compared with that of the pristine PI matrix, the enhancement of T_5 of the CMG/PI nanocomposite with 5 wt% CMG is 18.6 °C, higher than those

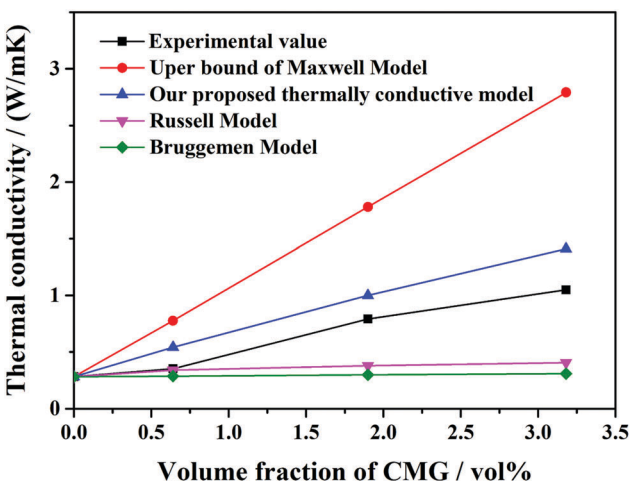

Fig. 10 Experimental λ values of the CMG/PI nanocomposites and theory λ values from our proposed thermal conductivity model, and the Maxwell, Russell and Bruggemen models.

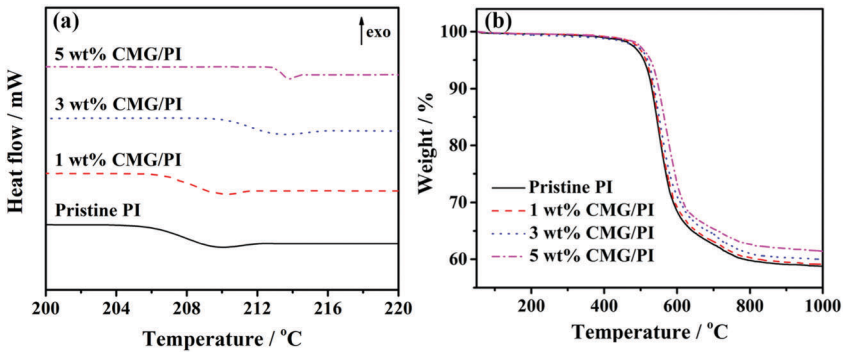

Fig. 11 DSC and TGA curves of the pristine PI matrix and CMG/PI nanocomposites. (a) DSC curves and (b) TGA curves.

Table 2 Characteristic thermal data of pristine PI matrix and the CMG/PI nanocomposites

		Weight loss temperature/°C		
Samples	T_g/°C	T_5	T_{30}	Heat-resistance index[a]/°C
Pristine PI	205.9	502.4	585.6	270.7
1 wt% CMG/PI	206.7	508.9	589.2	273.0
3 wt% CMG/PI	209.9	516.1	605.2	279.1
5 wt% CMG/PI	213.0	521.0	612.9	282.3

[a] $T_{\text{Heat-resistance index}} = 0.49 \times [T_5 + 0.6 \times (T_{30} - T_5)]$. T_5 and T_{30} is corresponding decomposition temperature of 5 wt% and 30 wt% weight loss, respectively.

of the previous reports about graphene/PI composites. For example, Liu *et al.*,[74] prepared reduced graphene oxide/polyimide (rGO/PI) films and the enhancement of T_5 of the film with 5 wt% rGO was about 10 °C. The main reason is that the introduction of CMG has a uniform dispersion in the PI matrix and forms a carbon layer network, to effectively hinder the effusion of decomposition products.[75] In addition, the introduction of CMG can limit the movement of the PI molecular chain. And the strong interaction between CMG and PI matrix can also increase the energy required for breaking the PI molecular chain at higher temperatures. Therefore, the ultimate thermal stabilities of the CMG/PI nanocomposites are enhanced.

4. Conclusion

The NH_2-POSS molecule has been grafted onto the surface of the GO. CMG could be obtained by the reaction between NH_2-POSS and GO, and could be evenly distributed on the surface of the PI fibers *via* electrospinning technology. The λ, α, T_g and T_{HRI} values of the CMG/PI nanocomposites were all increased with increasing the CMG loading. The λ and α values of the CMG/PI nanocomposite with 5 wt% CMG were significantly improved to 1.05 W m^{-1} K^{-1} and 0.98 mm^2 s^{-1}, about 4 times that of the pristine PI matrix (λ of 0.28 W m^{-1} K^{-1} and α of 0.24 mm^2 s^{-1}), respectively. Infrared thermal images of the CMG/PI nanocomposites further revealed that the CMG maintained a macroscopic uniform dispersibility. The corresponding T_g and T_{HRI} values of the CMG/PI nanocomposite with 5 wt% CMG were also enhanced to 213.0 and 282.3 °C, respectively. In addition, the obtained calculated λ values by our proposed thermal conductivity model were more consistent with the experimental λ values than those of the Maxwell, Russell and Bruggemen theory models. Our proposed fabrication method can be used to realize high thermal conductivities of the polymeric matrix by adding a relatively lower loading of thermally conductive fillers. Furthermore, our proposed thermal conductivity model can be promising to calculate the effective thermal conductivity coefficient (ETC) of anisotropic polymeric nanocomposites.

Conflicts of interest

There are no conflicts to declare.

Acknowledgements

The authors are grateful for the support and funding from the National Natural Science Foundation of China (No. 51773169, 51403175 and 81400765); the Open Fund from State Key Laboratory of Solid Lubrication of Lanzhou Institute of Chemical Physics (LSL-1715); the Fundamental Research Funds for the Central Universities (No. 3102017jg02003); the State Key Laboratory of Solidification Processing in NPU (No. SKLSP201713); K. Ruan thanks the Undergraduate Innovation & Business Program in Northwestern Polytechnical University (No. 201710699268 and 201710699382).

References

1 X. Huang, C. Zhi, P. Jiang, D. Golberg, Y. Bando and T. Tanaka, *Adv. Funct. Mater.*, 2013, **23**, 1824–1831.

2 H. Deng, L. Lin, M. Ji, S. Zhang, M. Yang and Q. Fu, *Prog. Polym. Sci.*, 2014, **39**, 627–655.
3 R. Wang and J. Wang, *Int. J. Heat Mass Transfer*, 2016, **99**, 750–761.
4 P. Ding, J. Zhang, N. Song, S. Tang, Y. Liu and L. Shi, *Compos. Sci. Technol.*, 2015, **109**, 25–31.
5 D. Jang, S. Yook and K. Lee, *Appl. Energy*, 2014, **116**, 260–268.
6 L. Chen, X. Hou, N. Song, L. Shi and P. Ding, *Composites, Part A*, 2018, **107**, 189–196.
7 E. Cho, J. Huang, C. Li, C. Chang-Jian, K. Lee, Y. Hsiao and J. Huang, *Carbon*, 2016, **102**, 66–73.
8 (*a*) J. Gu, Y. Guo, Z. Lv, W. Geng and Q. Zhang, *Composites, Part A*, 2015, **78**, 95–101; (*b*) L. Mu, J. He, Y. Li, T. Ji, N. Mehra, Y. Shi and J. Zhu, *J. Phys. Chem. C*, 2017, **121**, 14204–14212.
9 H. Zhang, Y. Lin, D. Zhang, W. Wang, Y. Xing, J. Lin, H. Hong and C. Li, *Curr. Appl. Phys.*, 2016, **16**, 1695–1702.
10 H. Zhou, H. Deng, L. Zhang and Q. Fu, *ACS Appl. Mater. Interfaces*, 2017, **9**, 29071–29081.
11 J. Gu, S. Xu, Q. Zhuang, Y. Tang and J. Kong, *IEEE Trans. Dielectr. Electr. Insul.*, 2017, **24**, 784–790.
12 J. Zha, Y. Zhu, W. Li, J. Bai and Z. Dang, *Appl. Phys. Lett.*, 2012, **101**, 062905.
13 (*a*) C. Feng, H. Ni, J. Chen and W. Yang, *ACS Appl. Mater. Interfaces*, 2016, **8**, 19732–19738; (*b*) L. Mu, Y. Li, N. Mehra, T. Ji and J. Zhu, *ACS Appl. Mater. Interfaces*, 2017, **9**, 12138–12145.
14 J. Gu, Y. Guo, X. Yang, C. Liang, W. Geng, L. Tang, N. Li and Q. Zhang, *Composites, Part A*, 2017, **95**, 267–273.
15 J. Yu, X. Huang, C. Wu, X. Wu, G. Wang and P. Jiang, *Polymer*, 2012, **53**, 471–480.
16 J. Gu, C. Liang, X. Zhao, B. Gan, H. Qiu, Y. Guo, X. Yang, Q. Zhang and D. Wang, *Compos. Sci. Technol.*, 2017, **139**, 83–89.
17 C. Feng, L. Bai, R. Bao, Z. Liu, M. Yang, J. Chen and W. Yang, *Adv. Compos. Hybrid Mater.*, 2018, **1**, 160–167.
18 J. Yang, P. Yu, L. Tang, R. Bao, Z. Liu, M. Yang and W. Yang, *Nanoscale*, 2017, **9**, 17704–17709.
19 (*a*) T. Wang, J. Yu, M. Wang, Y. Cao, W. Dai, D. Shen, L. Guo, Y. Wu, H. Bai and D. Dai, *Compos. Commun.*, 2017, **5**, 46–53; (*b*) N. Mehra, L. Mu, T. Ji, Y. Li and J. Zhu, *Compos. Sci. Technol.*, 2017, **151**, 115–123.
20 B. Zhu, J. Wang, H. Zheng, J. Ma, J. Wu and R. Wu, *Composites, Part B*, 2015, **69**, 496–506.
21 (*a*) W. Zhao, J. Kong, H. Liu, Q. Zhuang, J. Gu and Z. Guo, *Nanoscale*, 2016, **8**, 19984–19993; (*b*) Y. Li, G. Xu, Y. Guo, T. Ma, X. Zhong, Q. Zhang and J. Gu, *Composites, Part A*, 2018, **107**, 570–578.
22 J. Zha, T. Zhu, Y. Wu, S. Wang, R. Li and Z. Dang, *J. Mater. Chem. C*, 2015, **3**, 7195–7202.
23 Z. Han and A. Fina, *Prog. Polym. Sci.*, 2011, **36**, 914–944.
24 Y. Hu, G. Du and N. Chen, *Compos. Sci. Technol.*, 2016, **124**, 36–43.
25 (*a*) W. Zhou, Y. Gong, L. Tu, L. Xu, W. Zhao, J. Cai, Y. Zhang and A. Zhou, *J. Alloys Compd.*, 2017, **693**, 1–8; (*b*) P. Kumar, F. Shahzad, S. Yu, S. Hong, Y. Kim and C. Koo, *Carbon*, 2015, **94**, 494–500.
26 (*a*) W. Zhou, Z. Wang, L. Dong, X. Sui and Q. Chen, *Composites, Part A*, 2015, **79**, 183–191; (*b*) J. Renteria, S. Ramirez, H. Malekpour, B. Alonso, A. Centeno, A. Zurutuza, A. Cocemasov, D. Nika and A. Balandin, *Adv. Funct. Mater.*, 2015, **25**, 4664–4672.
27 J. Huang, Y. Zhu, L. Xu, J. Chen, W. Jiang and X. Nie, *Compos. Sci. Technol.*, 2016, **129**, 160–165.
28 N. Bagotia, V. Choudhary and D. Sharma, *Composites, Part B*, 2017, **124**, 101–110.
29 (*a*) X. Wang, X. Liu, H. Yuan, H. Liu, C. Liu, T. Li, C. Yan, X. Yan, C. Shen and Z. Guo, *Mater. Des.*, 2018, **139**, 372–379; (*b*) C. Wang, M. Zhao, J. Li, J. Yu, S. Sun, S. Ge, X. Guo, F. Xie, B. Jiang, E. Wujcik, Y. Huang, N. Wang and Z. Guo, *Polymer*, 2017, **131**, 163–271; (*c*) F. Ren, D. Song, Z. Li, L. Jia, Y. Zhao, D. Yan and Y. Ren, *J. Mater. Chem. C*, 2018, **6**, 1476–1486; (*d*) K. Sun, P. Xie, Z. Wang, T. Su, Q. Shao, J. Ryu, X. Zhang, J. Guo, A. Shankar, J. Li, R. Fan, D. Cao and Z. Guo, *Polymer*, 2017, **125**, 50–57.
30 Z. Hu, C. Wang, F. Zhao, X. Xu, S. Wang, L. Yu, D. Zhang and Y. Huang, *Nanoscale*, 2017, **9**, 8825–8833.
31 Z. Hu, D. Zhang, L. Yu and Y. Huang, *J. Mater. Chem. B*, 2018, **6**, 518–526.
32 M. Lahelin, M. Annala, A. Nykänen, J. Ruokolainen and J. Seppälä, *Compos. Sci. Technol.*, 2011, **71**, 900–907.
33 (*a*) H. Shin, Y. Li, A. Paynter, K. Nartetamrongsutt and G. Chase, *Polymer*, 2015, **65**, 26–33; (*b*) L. Zhang, W. Yu, C. Han, J. Guo, Q. Zhang, H. Xie, Q. Shao, Z. Sun and Z. Guo, *J. Electrochem. Soc.*, 2017, **164**, H651–H656; (*c*) L. Zhang, M. Qin, W. Yu, Q. Zhang, H. Xie, Z. Sun, Q. Shao, X. Guo, L. Hao, Y. Zheng and Z. Guo, *J. Electrochem. Soc.*, 2017, **164**, H1086–H1090; (*d*) J. Huang, Y. Cao, Q. Shao, X. Peng and Z. Guo, *Ind. Eng. Chem. Res.*, 2017, **56**, 10689–10701; (*e*) Y. Li, B. Zhou, G. Zheng, X. Liu, T. Li, C. Yan, C. Cheng, K. Dai, C. Liu, C. Shen and Z. Guo, *J. Mater. Chem. C*, 2018, **6**, 2258–2269.
34 S. McCullen, D. Stevens, W. Roberts, S. Ojha, L. Clarke and R. Gorga, *Macromolecules*, 2007, **40**, 997–1003.
35 T. Jiang, E. Carbone, K. Lo and C. Laurencin, *Prog. Polym. Sci.*, 2015, **46**, 1–24.
36 J. Gu, Z. Lv, Y. Wu, Y. Guo, L. Tian, H. Qiu, W. Li and Q. Zhang, *Composites, Part A*, 2017, **94**, 209–216.
37 Y. Lu, J. Hao, G. Xiao, H. Zhao, Z. Hu and T. Wang, *Appl. Surf. Sci.*, 2017, **394**, 78–86.
38 A. Askalany, S. Henninger, M. Ghazy and B. Saha, *Appl. Therm. Eng.*, 2017, **110**, 695–702.
39 M. Qian, V. Murray, W. Wei, B. Marshall and T. Minton, *ACS Appl. Mater. Interfaces*, 2016, **8**, 33982–33992.
40 Y. Ding, H. Hou, Y. Zhao, Z. Zhu and H. Fong, *Prog. Polym. Sci.*, 2016, **61**, 67–103.
41 L. Xu, G. Chen, W. Wang, L. Li and X. Fang, *Composites, Part A*, 2016, **84**, 472–481.
42 C. Lin, I. Lin and W. Tuan, *J. Mater. Sci.*, 2017, **52**, 1759–1766.
43 C. Rao, A. Sood, K. Subrahmanyam and A. Govindaraj, *Angew. Chem., Int. Ed.*, 2009, **48**, 7752–7777.

44 (*a*) M. Suominen, P. Damlin, S. Granroth and C. Kvarnstrom, *Carbon*, 2018, **128**, 205–214; (*b*) J. Zhang, Y. Liang, X. Wang, H. Zhou, S. Li, J. Zhang, Y. Feng, N. Lu, Q. Wang and Z. Guo, *Adv. Compos. Hybrid Mater.*, 2018, DOI: 10.1007/s42114-017-0007-0.
45 D. Dreyer, S. Park, C. Bielawski and R. Ruoff, *Chem. Soc. Rev.*, 2009, **39**, 228–240.
46 Z. Li, R. Wang, R. Young, L. Deng, F. Yang, L. Hao, W. Jiao and W. Liu, *Polymer*, 2013, **54**, 6437–6446.
47 Y. Sun, Z. Fang, C. Wang, K. Ariyawansha, A. Zhou and H. Duan, *Nanoscale*, 2015, **7**, 7790–7801.
48 W. Yu, J. Fu, X. Dong, L. Chen and L. Shi, *Compos. Sci. Technol.*, 2014, **92**, 112–119.
49 M. Wahlander, F. Nilsson, A. Carlmark, U. Gedde, S. Edmondson and E. Malmstrom, *Nanoscale*, 2016, **8**, 14730–14745.
50 W. Zhang and A. Müller, *Prog. Polym. Sci.*, 2013, **38**, 1121–1162.
51 Y. Xue, Y. Liu, F. Lu, J. Qu, H. Chen and L. Dai, *J. Phys. Chem. Lett.*, 2012, **3**, 1607–1612.
52 H. Li, S. Dai, J. Miao, X. Wu, N. Chandrasekharan, H. Qiu and J. Yang, *Carbon*, 2018, **126**, 319–327.
53 G. Wu, Y. Cheng, Z. Wang, K. Wang and A. Feng, *J. Mater. Sci.: Mater. Electron.*, 2017, **28**, 576–581.
54 Y. Xu, L. Zhao, H. Bai, W. Hong, C. Li and G. Shi, *J. Am. Chem. Soc.*, 2009, **131**, 13490–13497.
55 W. Liao, S. Yang, S. Hsiao, Y. Wang, S. Li, C. Ma, H. Tien and S. Zeng, *ACS Appl. Mater. Interfaces*, 2014, **6**, 15802–15812.
56 D. Li, M. Müller, S. Gilje, R. Kaner and G. Wallace, *Nat. Nanotechnol.*, 2008, **3**, 101–105.
57 L. Malard, M. Pimenta, G. Dresselhaus and M. Dresselhaus, *Phys. Rep.*, 2009, **473**, 51–87.
58 Y. Li, H. Zhang, H. Porwal, Z. Huang, E. Bilotti and T. Peijs, *Composites, Part A*, 2017, **95**, 229–236.
59 F. Alam, W. Dai, M. Yang, S. Du, X. Li, J. Yu, N. Jiang and C. Lin, *J. Mater. Chem. A*, 2017, **5**, 6164–6169.
60 M. Saeidijavash, J. Garg, B. Grady, B. Smith, Z. Li, R. Young, F. Tarannum and N. Bekri, *Nanoscale*, 2017, **9**, 12867–12873.
61 S. Song and Y. Zhang, *Carbon*, 2017, **123**, 158–167.
62 Z. Liu, H. Zhang, S. Song and Y. Zhang, *Compos. Sci. Technol.*, 2017, **150**, 174–180.
63 M. Chau, B. Kopera, V. Machado, S. Tehrani, M. Winnik, E. Kumacheva and M. Retsch, *Mater. Horiz.*, 2017, **4**, 236–241.
64 M. Safdari, M. Baniassadi, H. Garmestani and M. Al-Haik, *J. Appl. Phys.*, 2012, **112**, 114318.
65 Q. Li, Y. Guo, W. Li, S. Qiu, C. Zhu, X. Wei, M. Chen, C. Liu, S. Liao, Y. Gong, A. Mishra and L. Liu, *Chem. Mater.*, 2014, **26**, 4459–4465.
66 A. Marconnett, N. Yamamoto, M. Panzer, B. Wardle and K. Goodson, *ACS Nano*, 2011, **5**, 4818–4825.
67 Z. Fan, F. Gong, S. Nguyen and H. Duong, *Carbon*, 2015, **81**, 396–404.
68 N. Song, D. Jiao, P. Ding, S. Cui, S. Tang and L. Shi, *J. Mater. Chem. C*, 2015, **4**, 305–314.
69 E. Swartz and R. Pohl, *Rev. Mod. Phys.*, 1989, **61**, 605–668.
70 D. Hahn and M. Özişik, *Heat Conduction in Anisotropic Solids*, John Wiley & Sons, Inc., New Jersey, 2012, vol. 15, pp. 614–650.
71 D. Ding, X. Yan, X. Zhang, Q. He, B. Qiu, D. Jiang, H. Wei, J. Guo, A. Umar, L. Sun, Q. Wang, M. Khan, D. Young, X. Zhang, B. Weeks, T. Ho, Z. Guo and S. Wei, *Superlattices Microstruct.*, 2015, **85**, 305–320.
72 J. Zhu, S. Wei, X. Chen, A. Karki, D. Rutman, D. Young and Z. Guo, *J. Phys. Chem. C*, 2010, **114**, 8844–8850.
73 J. Gu, W. Dong, S. Xu, Y. Tang, L. Ye and J. Kong, *Compos. Sci. Technol.*, 2017, **144**, 185–192.
74 H. Yang, Z. Li, H. Zou and P. Liu, *Polym. Adv. Technol.*, 2017, **28**, 233–242.
75 H. Ha, A. Choudhury, T. Kamal, D. Kim and S. Park, *ACS Appl. Mater. Interfaces*, 2012, **4**, 4623–4630.